

# First-principles Calculation of the Temperature-dependent Transition Energies in Spin Defects

Hao Tang,<sup>1,\*</sup> Ariel Rebekah Barr,<sup>1,\*</sup> Guoqing Wang,<sup>2,3,\*</sup> Paola Cappellaro,<sup>2,3,4,†</sup> and Ju Li<sup>1,3,‡</sup>

<sup>1</sup>*Department of Materials Science and Engineering,  
Massachusetts Institute of Technology, MA 02139, USA*

<sup>2</sup>*Research Laboratory of Electronics, Massachusetts Institute of Technology, Cambridge, MA 02139, USA*

<sup>3</sup>*Department of Nuclear Science and Engineering,  
Massachusetts Institute of Technology, Cambridge, MA 02139, USA*

<sup>4</sup>*Department of Physics, Massachusetts Institute of Technology, Cambridge, MA 02139, USA*

(Dated: September 8, 2022)

Spin qubits associated with color centers are promising platforms for various quantum technologies. However, to be deployed in robust quantum devices, the variations of their intrinsic properties with the external conditions, and in particular temperature, should be known with high precision. Unfortunately, a predictive theory on the temperature dependence of the resonance frequency of electron and nuclear spin defects in solids remains lacking. In this work, we develop a first-principles method for the temperature dependence of zero-field splitting, hyperfine interaction, and nuclear quadrupole interaction of color centers. As a testbed, we compare our ab-initio calculation results with experiments in the Nitrogen-Vacancy (NV) center finding good agreement. Interestingly, we identify the major origin of the temperature dependence as a second-order effect of phonon vibration. The method is generally applicable to different color centers and provides a theoretical tool for designing high-precision quantum sensors.

Color centers, the fluorescent lattice defects in insulators, have been intensively studied as solid-state qubits for quantum computing [1, 2], quantum communication [3, 4], and quantum sensing [5, 6]. The temperature (and strain) dependence of the spin defects properties is a critical factor in their performance: their spatio-temporal fluctuations in the crystal host would result in degraded coherence times, while the sensitivity of the defects to small variations can be exploited in quantum sensing [5]. A predictive theoretical model accompanied by a robust computational protocol would be invaluable in both mitigating deleterious effects and selecting the best host/defects combinations for quantum sensing. Here, we developed a first-principles method for predicting the temperature dependence of optical, electronic and nuclear spin transition frequencies. We benchmark our calculations using the properties of the nitrogen-vacancy (NV) center in diamond. Our first-principle calculations achieve excellent agreement with the temperature dependence of the NV zero phonon line (ZPL), zero-field splitting (ZFS), hyperfine interaction and nuclear quadrupole interaction. Crucially, we find that the dominant part of the temperature dependence is from a second-order dynamical phonon effect. Our method paves the way for computation-assisted design of novel quantum sensors using color centers in solids.

We select the NV center as our testbed since it has been accurately characterized in experiments for its applications to quantum sensing of magnetic fields [7, 8], electric fields [9], temperature [10, 11], pressure [12, 13], and rotation [14, 15]. While the temperature dependence of the NV electronic spin resonance frequency [16] has been exploited to probe the local temperature with ultra-high

spatial resolution in nanothermometry devices [17–24], it is also detrimental to some quantum devices since its fluctuations can lead to decoherence [25].

Despite extensive experimental study on the temperature dependence of both electronic and nuclear spin frequencies [26–31], a predictive theoretical method is still lacking. The temperature dependence has been previously attributed to thermal expansion, but the calculated temperature shifts are far smaller in absolute magnitude than the experimental values [26, 30–32] (in all cases by an order of magnitude). This discrepancy indicates that other effects dominate the temperature dependence. Various explanations have been proposed for such a discrepancy. Doherty *et al.* proposed that the dynamical phonon effect might play an important role in the temperature dependence of the ZFS [16]. However, in the absence of a method to evaluate the dynamical phonon effect from first principles, its contribution to the temperature dependence could not be unambiguously determined. To overcome these challenges, here we develop a theoretical model of the defect energy transitions  $\nu$  dependence on the temperature-induced atomic displacement up to second order. We combine a full calculation of the phonon spectrum including density functional perturbation theory (DFPT) [33] with density functional theory (DFT) calculation of the spin-transition energies with the supercell method [34].

Given an electro-nuclear spin system, such as the NV center, we aim at calculating the temperature-induced shift of a transition frequency  $\nu$  between any two levels that can be probed experimentally (e.g., by Rabi experiments.) The shift in  $\nu$  arises from the temperature-induced atomic displacement, as the thermal excitation

of electrons is negligible due to the large energy gap in a broad temperature range. For a general transition, the atomic displacement effect is described by the energy surfaces of the two levels as a function of atomic coordinates, as shown in Fig. 1(a). Expressing the atomic configuration by the normal coordinates of phonon modes  $\{q_i\}$ , the transition frequency is then a function of  $(\{q_i\})$ :  $\nu = [E_2(\{q_i\}) - E_1(\{q_i\})]/\hbar$  ( $E_1$  and  $E_2$  are the energy level 1 and energy level 2, respectively). At finite temperature,  $\{q_i\}$  have both thermal and quantum fluctuations. As all electron and nuclear spin transition frequencies are at least three orders of magnitude smaller than the typical phonon frequency [35], the measured  $\nu$  is a statistical average of the phonon mode distribution:

$$\langle \nu \rangle = \nu_0 + \sum_i \left[ \left( \frac{\partial \nu}{\partial q_i} \right)_0 \langle q_i \rangle + \frac{1}{2} \left( \frac{\partial^2 \nu}{\partial q_i^2} \right)_0 \langle q_i^2 \rangle \right] + O(q^3). \quad (1)$$

The first-order term represents the change of atomic equilibrium positions, corresponding to thermal expansion. Here we emphasize that the first-order term is typically smaller than the second-order term as  $\langle q_i \rangle$  originates from the weak phonon anharmonicity. Then, what appears to be a “first-order term” in Eq. (1) is actually the product of first-order and third-order terms, as a purely harmonic system will have zero thermal expansion with  $\langle q_i \rangle = 0$ . We evaluate the first-order term through the quasiharmonic approximation [36] as a static lattice expansion effect. The temperature-dependent lattice parameter  $a(T)$  of nitrogen-rich diamond is reproduced from the previous experiments [37], and  $\nu(a)$  is calculated for different  $a$  at equilibrium atomic configuration. The thermal expansion contribution to the spectral drift is then:

$$\left( \frac{\partial \nu}{\partial T} \right)_{\text{quasiharmonic}} = \frac{\partial \nu}{\partial a} a(T) \alpha(T), \quad (2)$$

where  $\alpha(T)$  is the linear thermal expansion coefficient at temperature  $T$ .

The dominant second-order term represents the atomic vibration around the equilibrium positions caused by phonon excitation at finite temperature. The second-order term is evaluated by the dependence of the spin-transition energy  $\nu$  on the phonon occupation number  $n_i = 0, 1, 2, \dots$  ( $i$  is the vibrational mode index), which affects  $\langle q_i^2 \rangle$  in Eq. (1). By evaluating  $\langle q_i^2 \rangle$  for a quantum harmonic oscillator (harmonic phonon theory) at thermal equilibrium,  $\langle q_i^2 \rangle = \frac{\hbar}{M_i \omega_i} (\langle n_i \rangle + \frac{1}{2}) = \frac{\hbar}{M_i \omega_i} \left( \frac{1}{e^{\hbar \omega_i / kT} - 1} + \frac{1}{2} \right)$ , we obtain

$$\langle \nu \rangle = \nu_0(a) + \sum_i \frac{1}{2} \frac{\partial^2 \nu}{\partial q_i^2} \frac{\hbar}{M_i \omega_i} \left( \frac{1}{e^{\hbar \omega_i / kT} - 1} + \frac{1}{2} \right), \quad (3)$$

where  $M_i$  is the mode-specific effective mass (conjugate to the  $q_i$  definition) in real-space harmonic lattice dynamics expansion. Here we already included the “first-order”, thermal expansion term in Eqs. (1)-(2) by taking

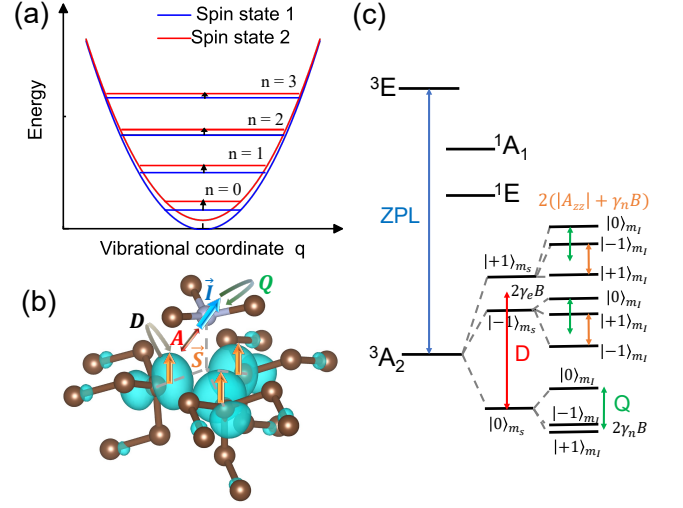


FIG. 1. (a) Illustration of the second-order phonon effect to spin resonance. (b) Electron and nuclear spin interaction in an NV center. The blue isosurface of electron spin density is from the DFT, and the brown and silver spheres represents carbon and nitrogen atoms, respectively. (c) The energy levels of NV centers.

$\nu_0$  not at the zero-temperature lattice constant  $a_0$ , but at finite-temperature lattice parameter  $\nu_0 = \nu_0(a(T))$ .

We can gain a physical intuition of this result by using the Franck–Condon principle [38] and graphically analyzing the expected frequency shift from Fig. 1(a). We consider two spin energy levels within vibrational energy levels ( $n_i = 0, 1, 2, \dots$ ) associated with orthogonal vibrational wavefunctions of the ions. The upper energy surface (red, associated with the higher spin energy) has a slightly softer phonon frequency (on average, at least, for the NV center). Therefore, the spin-transition energy  $\nu$  decreases as the phonon number  $n_i$  increases. Although the typical radio-frequency and microwave (MHz to GHz) spin control cannot induce direct transitions between different phonon levels  $n_i$  ( $\sim$ THz), these vibration energy levels still affect the average spin transition frequencies by inducing a relatively small shifts in total energy ( $n_i + \frac{1}{2}$ ) $\hbar\Delta\omega_i$ , where  $\Delta\omega_i = \omega_i^{\text{red}} - \omega_i^{\text{blue}}$  is the difference in modal frequency between the upper energy surface (red) and the lower energy surface (blue).

More specifically, the mean value of the spin transition frequency can be calculated as

$$\begin{aligned} \langle \nu \rangle &= \sum_{\{n_i\}} \frac{e^{-\sum_i \hbar \omega_i (n_i + \frac{1}{2}) / (kT)}}{Z} \left[ \nu_0(a) + \sum_i \frac{\Delta\omega_i}{2\pi} (n_i + \frac{1}{2}) \right] \\ &= \nu_0(a) + \sum_i \frac{\Delta\omega_i}{2\pi} \left( \frac{1}{e^{\hbar \omega_i / (kT)} - 1} + \frac{1}{2} \right). \end{aligned} \quad (4)$$

As  $\Delta\omega_i \ll \omega_i \equiv (\omega_i^{\text{red}} + \omega_i^{\text{blue}})/2$ , the expression can be evaluated by the second order derivative of the spin-transition energy (vertical distance between red and blue)

to the normal-mode coordinates  $\Delta\omega_i = \frac{\hbar}{2M_i\omega_i} \frac{\partial^2(2\pi\nu)}{\partial q_i^2}$ , where  $(2\pi\hbar\nu)$  is the difference in red and blue potential energy surfaces. Then the temperature-dependent frequency due to dynamic-harmonic-phonon effect is given by Eq. (3), which is the form we will adopt for the numerical computations in this paper.

Based on the theoretical analysis, we develop the first-principles method to evaluate the quantities in Eq. (3). At first, a full phonon calculation is implemented through the phonopy package [39] combined with DFPT implemented in Vienna ab-initio simulation package (VASP) [40, 41] to derive the frequency  $\omega_i$  and effective mass  $M_i$  of the full phonon spectrum. The second-order derivatives are then calculated by the finite-differential method:

$$\frac{\partial^2\nu}{\partial q_i^2} = \frac{1}{\delta q_i^2} [\nu(\delta q_i) + \nu(-\delta q_i) - 2\nu(0)] + \mathcal{O}(\delta q_i^2), \quad (5)$$

where  $\nu(q_i)$  is calculated by exerting a small displacement of  $\delta q_i$  relative to the relaxed atomic configuration in the DFT calculations (see Supplemental Materials for details [42]).

We simulate the NV center in diamond by a  $4 \times 4 \times 4$  rhombohedral supercell with the single defect at the center. First, we calculate the zero-temperature electronic structures of the NV center for the fully relaxed atomic configuration (Fig. 1b). The electronic structure calculation employs the DFT and projector-augmented-wave (PAW) method implemented by VASP. The ground state  ${}^3A_2$  contains electron spin  $S = 1$  and  ${}^{14}\text{N}$  nuclear spin  $I = 1$ , leading to the fine and hyperfine structure shown in Fig. 1(c). The spin state splittings originate from three types of interaction: the electron-electron magnetic dipolar interaction  $\mathbf{D}$ , the hyperfine interaction  $\mathbf{A}$ , and the nuclear quadrupole interaction  $\mathbf{Q}$  [43]:

$$\hat{H} = \vec{S} \cdot \mathbf{D} \cdot \vec{S} + \vec{S} \cdot \mathbf{A} \cdot \vec{I} + \vec{I} \cdot \mathbf{Q} \cdot \vec{I}. \quad (6)$$

$\mathbf{D}$ ,  $\mathbf{A}$ , and  $\mathbf{Q}$  are calculated by the  $1^{st}$ -order perturbation theory to the DFT ground state [32, 44–47] (see SM [42] for details). Selecting the  $C_3$  axis of the NV center as the  $z$ -direction, and taking into account that  $H_D \gg H_A, H_Q$ , the effective Hamiltonian reduces to [35]

$$\hat{H} = DS_z^2 + QI_z^2 + A_{zz}S_zI_z, \quad (7)$$

where  $D = \frac{3}{2}D_{zz}$  and  $Q = \frac{3}{2}Q_{zz}$ . The temperature variations of  $D$ ,  $Q$ , and  $A_{zz}$  are then calculated by relating them to transitions  $\nu$  between two selected spin states (illustrated in Fig. 1c). Similarly, the ZPL's temperature dependence is calculated by Eq. (4) using the  $\Delta$ SCF method [44, 48, 49] (see SM [42] for details).

Applying our method to electronic transition, we calculate the temperature dependence of the ZPL and ZFS (Fig. 2). The “first-order” thermal expansion effect is, as found in previous computational work [26, 32], far

smaller than the experimental results for the measured temperature drifts. This is not surprising since the quasi-harmonic “first-order” is physically a “cubic-order” Grüneisen parameter  $\times$  “first-order” effect. Including the second-order dynamical phonon effects corrects the discrepancy. The overall simulation results (summation of the first and second-order) for both quantities are now consistent with prior experimental results. The calculated temperature derivative  $\frac{dD}{dT}$  at room temperature is  $-75.99$  kHz/K, consistent with the widely used experimental value of  $-74.27$  kHz/K [26]. Different from Ref. [16] where the dynamical phonon effect is fitted by experiment, we evaluate the effect in a parameter-free manner from first-principles calculations. Our result strongly indicates that the main mechanisms of the temperature dependence of the ZPL and ZFS is the dynamical phonon effect, with a smaller contribution from the thermal expansion. The temperature shift of the ZFS in NV centers provides promising prospects for nanothermometry, where the magnitude of  $\frac{dD}{dT}$  is crucial for its temperature sensitivity [6]. Our method provides a predictive tool to search for different color centers for optimal temperature sensitivity.

We then calculate the temperature dependence of the nuclear spin interaction. The temperature dependence of  ${}^{14}\text{N}$ -related nuclear spin transition is shown in Figs. 3(a,b). Both  $A_{zz}$  and  $Q$  are negative quantities,

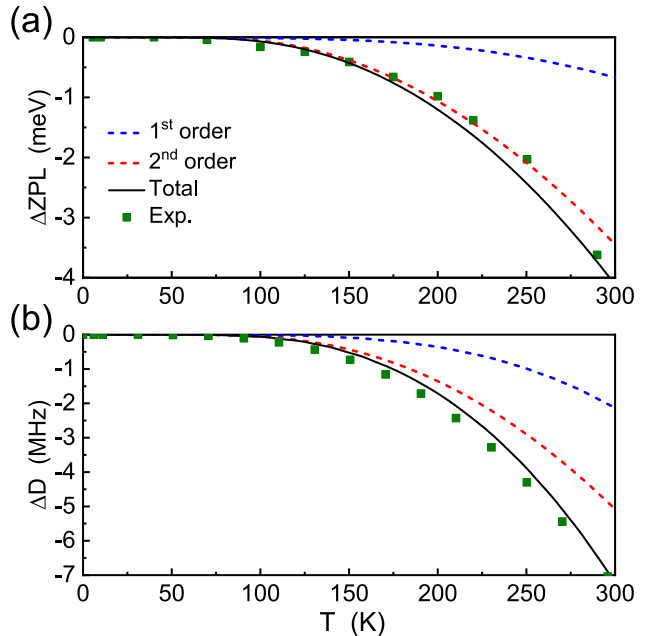


FIG. 2. (a) The ZPL and (b) ZFS from simulation and experiment. The blue and red dashed lines represent the first-order (thermal expansion) and second-order (dynamical phonon) effects, respectively. The black line is the total shift from simulation, and the green dots are experimental data points reproduced from Refs. [16, 30]

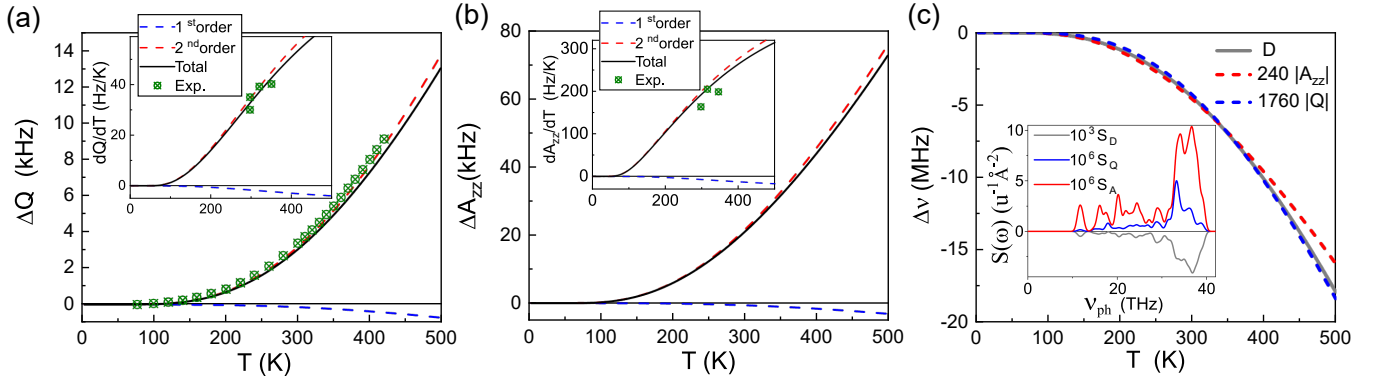


FIG. 3. (a) Nuclear quadrupole interaction  $Q$  and (b) Hyperfine interaction  $A_{zz}$  from simulation. The blue, red, and black curves represent the calculated temperature-induced change from thermal expansion effect, 2<sup>nd</sup>-order vibration effect, and their summation, respectively. The insets are the derivative of  $Q$  and  $A_{zz}$  results, where the green dots are experimental data reproduced from ref. [16, 27, 28, 50] (c) Overlap behavior of  $D(T)$ ,  $Q(T)$ , and  $A_{zz}(T)$  from simulation. The inset shows the spectral density  $S_D$ ,  $S_Q$ , and  $S_A$  as defined in Eq. (8), where Gaussian broadening is applied to the  $\delta(\omega - \omega_i)$  for each phonon mode with a width of 2 THz.

and their absolute values decrease with increasing temperature, yielding positive  $dQ/dT$  and  $dA_{zz}/dT$ . The thermal expansion contribution to the temperature shifts has an opposite slope with respect to the experiments. The dynamical phonon effect is more than one order of magnitude larger than the thermal expansion effects, so it corrects both the trend and the magnitude, obtaining  $\frac{dQ}{dT}$  and  $\frac{dA_{zz}}{dT}$  in good agreement with the previous experiments [16, 27, 28, 50].

$A_{zz}$  is much more sensitive to  $T$  than  $Q$ . The sensitivity of  $A_{zz}$  mainly comes from the Fermi contact term that is highly sensitive to the atomic displacement in the dynamical phonon effects according to our calculations. In comparison, the electric field gradient (EFG) is relatively insensitive to atomic displacement, so  $Q$  has a smaller temperature shift. Therefore, we expect that the higher sensitivity of  $A_{zz}$  than  $Q$  is also a general behavior in many other color centers. It has been recently proposed that with  $\frac{dA_{zz}}{dQ} > 1$ , the coherence time of nuclear spin qubits can be robustly protected by at least one order of magnitude through noise decoupling techniques [50]. The generality of the higher sensitivity of  $A_{zz}$  indicates a broad applicability of such a method to various solid state spin defects. The relative shift of the hyperfine transition,  $\frac{dA_{zz}}{dT} \frac{1}{A_{zz}}$  approaches  $8.9 \times 10^{-5} K^{-1}$  at room temperature. While the absolute value of ZFS shift is much larger, the relative frequency change  $\frac{dD}{dT} \frac{1}{D} \approx 2.58 \times 10^{-5}$  is smaller than for the hyperfine. Thus, to operate a quantum sensor based on the nuclear spin it is imperative to re-calibrate the temperature effects [25].

Previous experimental results had observed a strong, but so-far unexplained, correlation between  $D(T)$  and  $Q(T)$  [28]. Our first-principles results not only confirm such a correlation and show its validity over a broad temperature range up to 500 K (Fig. 3c), but also provide approaches to revealing the underlying mechanism of such

a correlation. As the dynamical phonon effects are dominant for all these interactions, we investigate the overlap behavior by defining the spectral density of the second-order derivative of  $\nu$  as

$$S_i(\omega) = \sum_j \frac{1}{M_j} \frac{\partial^2 \nu_i}{\partial q_j^2} \delta(\omega - \omega_i), \quad (8)$$

as shown in the inset of Fig. 3(c). The large intensities of  $S_D$ ,  $S_Q$ , and  $S_A$  at around 32 ~ 38 THz is attributed to the high phonon density of states (DOS) [51] and large second-order derivatives in Eq. (8) at that frequency range. The ratio between two temperature-induced frequency shifts is then a weighted average between their spectral density:

$$\frac{\Delta \nu_1}{\Delta \nu_2} = \frac{\int S_1(\omega) f_{\text{FD}}(T, \omega) / \omega d\omega}{\int S_2(\omega) f_{\text{FD}}(T, \omega) / \omega d\omega}, \quad (9)$$

where  $f_{\text{FD}}$  is the Fermi-Dirac distribution. As the spectral densities  $S_Q$  and  $S_D$  have a similar shape, the ratio  $\Delta Q/\Delta D$  is relatively insensitive to temperature. In comparison,  $S_A$  shows a more striking difference, undermining  $A_{zz}$ 's overlap with  $Q$  and  $D$ . Thus, although  $A_{zz}(T)$  also shows an approximate correlation with  $Q$  and  $D$ , it has a relatively larger deviation with a larger slope in the low-temperature region and a smaller slope in the high-temperature region as shown in Fig. 3(c). We note that the spectral correlation between different interactions can be quite accurate and paves the way to designing robust coherence protection protocols by refocusing one interaction variations using other correlated interactions over a broad range of temperatures [50].

Beyond accurately reproducing experimental results, we can predict the hyperfine temperature shift of  $^{13}\text{C}$  nuclear spins around the NV center, which have been actively investigated as qubits [29, 52–55] (Fig. 4a).  $A_{zz}$  for



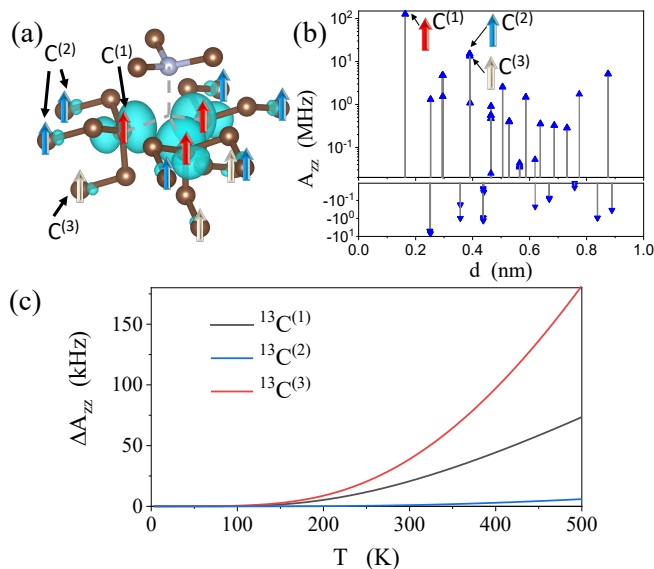


FIG. 4. Hyperfine interaction  $A_{zz}$  with  $^{13}\text{C}$  nuclear spin from simulation. (a) Illustration of the three groups of identical nuclear spins with the strongest hyperfine interaction. (b)  $A_{zz}$  for different  $^{13}\text{C}$  nuclear spin around the NV center plotted against the distance  $d$  between the  $^{13}\text{C}$  site and the NV center. (c) Temperature shifts of  $A_{zz}$  for  $^{13}\text{C}$  atoms at different sites.

$^{13}\text{C}$  atoms at different lattice sites around the NV centers is shown in Fig. 4b as a function of their distance to the NV center, where we identify three groups of equivalent  $^{13}\text{C}$  lattice sites with the strongest interaction. The  $^{13}\text{C}$  atom at the first-shell lattice sites ( $\text{C}^{(1)}$ ) of the NV center shows a strong hyperfine splitting of 129 MHz, well consistent with the experimental value of 127 MHz [29].

The temperature dependence  $\Delta A_{zz}(T)$  of the three groups of  $^{13}\text{C}$  lattice sites is shown in Fig. 4c.  $A_{zz}$  is positively related to  $T$  for all the three groups of lattice sites. The most sensitive temperature dependence appears for  $\text{C}^{(3)}$  lattice sites, where the temperature shift approaches 47.2 kHz at 300 K. At room temperature, the slope  $dA_{zz}/dT$  for  $\text{C}^{(1)}$ ,  $\text{C}^{(2)}$ , and  $\text{C}^{(3)}$  are 201, 14, 440 Hz/K, respectively. Previously, experimental work on the temperature dependence of  $^{13}\text{C}$  hyperfine interaction did not provide definite results due to the high noise, while their computational study did not consider the second-order dynamical phonon effect [29]. Our results provide a theoretical prediction for  $A_{zz}(T)$  of  $^{13}\text{C}$  atoms in NV centers, which could be measured by the nuclear spin transition [50].

In the discussion above, we focus on the temperature shift under thermal equilibrium, but the dynamical phonon effect on spin transition frequency can be extended to kinetic processes such as phonon transport. In general, the temperature shift at a single NV center measures a linear combination  $\hat{O}(r) = \sum_i \frac{\hbar}{2M_i\omega_i} \frac{\partial^2 \nu}{\partial q_i^2} \hat{n}_i(\vec{r})$  of the particle number operators  $\hat{n}_i$  of ambient phonon, where electron or nuclear spin of an NV ensemble can

probe phonon distribution in the sample. While most materials characterization methods probe the atomic equilibrium position, the second-order temperature shift of spin defects provides a potential way to probe the dynamical process of local atomic vibrations.

Our work provides a general scheme to study the temperature dependence of transition frequencies of color centers. An integrated python program interfaces with VASP and phonopy will be made publicly accessible, which can carry out the numerical workflow automatically. Besides the NV center, various other color centers such as SiV, SnV, PbV, GeV, MgV in diamond are also widely studied due to their potential in quantum sensing and communication [5, 56–58]. Besides diamond, point defects in silicon [59–61], silicon-carbide [62–64],  $\text{Y}_2\text{SiO}_5$  [65], and  $\text{YVO}_4$  [66, 67] also attract broad interests. The temperature dependence data of transition frequency remains lacking for many of these systems. Applying our method to these spin defects can establish a database for temperature-dependent transition frequency of electronic excitation, electron and nuclear spin transitions, which provides critical information for searching and designing high-performance quantum devices such as highly-sensitive sensors and long-lived memories. Thus, our result paves the way to perform a systematic study on the energy levels of point defects targeted for different quantum applications.

We thank Haowei Xu, Boning Li, and Yixuan Song for insightful discussions. This work was supported by HRI-US, NSF DMR-1923976, NSF DMR-1923929 and NSF CMMI-1922206. A.R.B. acknowledges support from a National Science Foundation Graduate Research Fellowship under Grant No. DGE-174530. The calculations in this work were performed in part on the Texas Advanced Computing Center (TACC) and MIT engaging cluster.

\* These authors contributed equally.

† pcappell@mit.edu

‡ liju@mit.edu

- [1] S. Pezzagna and J. Meijer, Quantum computer based on color centers in diamond, *Applied Physics Reviews* **8**, 011308 (2021).
- [2] N. P. de Leon, K. M. Itoh, D. Kim, K. K. Mehta, T. E. Northup, H. Paik, B. Palmer, N. Samarth, S. Sangtawesin, and D. Steuerma, Materials challenges and opportunities for quantum computing hardware, *Science* **372**, eabb2823 (2021).
- [3] W. Pfaff, B. J. Hensen, H. Bernien, S. B. van Dam, M. S. Blok, T. H. Taminiau, M. J. Tiggelman, R. N. Schouten, M. Markham, D. J. Twitchen, *et al.*, Unconditional quantum teleportation between distant solid-state quantum bits, *Science* **345**, 532 (2014).
- [4] L. Childress, J. Taylor, A. S. Sørensen, and M. Lukin, Fault-tolerant quantum communication based on solid-state photon emitters, *Physical review letters* **96**, 070504

- (2006).
- [5] C. L. Degen, F. Reinhard, and P. Cappellaro, Quantum sensing, *Reviews of modern physics* **89**, 035002 (2017).
  - [6] R. Schirhagl, K. Chang, M. Loretz, and C. L. Degen, Nitrogen-vacancy centers in diamond: nanoscale sensors for physics and biology, *Annual review of physical chemistry* **65**, 83 (2014).
  - [7] S. Hong, M. S. Grinolds, L. M. Pham, D. Le Sage, L. Luan, R. L. Walsworth, and A. Yacoby, Nanoscale magnetometry with nv centers in diamond, *MRS bulletin* **38**, 155 (2013).
  - [8] J. F. Barry, J. M. Schloss, E. Bauch, M. J. Turner, C. A. Hart, L. M. Pham, and R. L. Walsworth, Sensitivity optimization for nv-diamond magnetometry, *Reviews of Modern Physics* **92**, 015004 (2020).
  - [9] F. Dolde, H. Fedder, M. W. Doherty, T. Nöbauer, F. Rempp, G. Balasubramanian, T. Wolf, F. Reinhard, L. C. Hollenberg, F. Jelezko, *et al.*, Electric-field sensing using single diamond spins, *Nature Physics* **7**, 459 (2011).
  - [10] N. Wang, G.-Q. Liu, W.-H. Leong, H. Zeng, X. Feng, S.-H. Li, F. Dolde, H. Fedder, J. Wrachtrup, X.-D. Cui, *et al.*, Magnetic criticality enhanced hybrid nanodiamond thermometer under ambient conditions, *Physical Review X* **8**, 011042 (2018).
  - [11] M. Fujiwara and Y. Shikano, Diamond quantum thermometry: From foundations to applications, *Nanotechnology* (2021).
  - [12] M. W. Doherty, V. V. Struzhkin, D. A. Simpson, L. P. McGuinness, Y. Meng, A. Stacey, T. J. Karle, R. J. Hemley, N. B. Manson, L. C. Hollenberg, *et al.*, Electronic properties and metrology applications of the diamond nv-center under pressure, *Physical review letters* **112**, 047601 (2014).
  - [13] K. O. Ho, M. Y. Leung, Y. Jiang, K. P. Ao, W. Zhang, K. Y. Yip, Y. Y. Pang, K. C. Wong, S. K. Goh, and S. Yang, Probing local pressure environment in anvil cells with nitrogen-vacancy (n-v) centers in diamond, *Physical Review Applied* **13**, 024041 (2020).
  - [14] A. Jarmola, S. Lourette, V. M. Acosta, A. G. Birdwell, P. Blümler, D. Budker, T. Ivanov, and V. S. Malinovsky, Demonstration of diamond nuclear spin gyroscope, *Science advances* **7**, eabl3840 (2021).
  - [15] V. V. Soshenko, S. V. Bolshedvorskii, O. Rubinas, V. N. Sorokin, A. N. Smolyaninov, V. V. Vorobyov, and A. V. Akimov, Nuclear spin gyroscope based on the nitrogen vacancy center in diamond, *Physical Review Letters* **126**, 197702 (2021).
  - [16] M. W. Doherty, V. M. Acosta, A. Jarmola, M. S. Barson, N. B. Manson, D. Budker, and L. C. Hollenberg, Temperature shifts of the resonances of the nv-center in diamond, *Physical Review B* **90**, 041201 (2014).
  - [17] P. Neumann, I. Jakobi, F. Dolde, C. Burk, R. Reuter, G. Waldherr, J. Honert, T. Wolf, A. Brunner, J. H. Shim, *et al.*, High-precision nanoscale temperature sensing using single defects in diamond, *Nano letters* **13**, 2738 (2013).
  - [18] H. Kraus, V. Soltamov, F. Fuchs, D. Simin, A. Sperlich, P. Baranov, G. Astakhov, and V. Dyakonov, Magnetic field and temperature sensing with atomic-scale spin defects in silicon carbide, *Scientific reports* **4**, 1 (2014).
  - [19] M. Alkahtani, I. Cojocaru, X. Liu, T. Herzig, J. Meijer, J. Küpper, T. Lühmann, A. V. Akimov, and P. R. Hemmer, Tin-vacancy in diamonds for luminescent thermometry, *Applied Physics Letters* **112**, 241902 (2018).
  - [20] C. T. Nguyen, R. E. Evans, A. Sipahigil, M. K. Bhaskar, D. D. Sukachev, V. N. Agafonov, V. A. Davydov, L. F. Kulikova, F. Jelezko, and M. D. Lukin, All-optical nanoscale thermometry with silicon-vacancy centers in diamond, *Applied Physics Letters* **112**, 203102 (2018).
  - [21] D. M. Toyli, F. Charles, D. J. Christle, V. V. Dobrovitski, and D. D. Awschalom, Fluorescence thermometry enhanced by the quantum coherence of single spins in diamond, *Proceedings of the National Academy of Sciences* **110**, 8417 (2013).
  - [22] G. Kucsko, P. C. Maurer, N. Y. Yao, M. Kubo, H. J. Noh, P. K. Lo, H. Park, and M. D. Lukin, Nanometre-scale thermometry in a living cell, *Nature* **500**, 54 (2013).
  - [23] T. Plakhotnik, M. W. Doherty, J. H. Cole, R. Chapman, and N. B. Manson, All-optical thermometry and thermal properties of the optically detected spin resonances of the nv-center in nanodiamond, *Nano letters* **14**, 4989 (2014).
  - [24] A. Gottscholl, M. Diez, V. Soltamov, C. Kasper, A. Sperlich, M. Kianinia, C. Bradac, I. Aharonovich, and V. Dyakonov, Sub-nanoscale temperature, magnetic field and pressure sensing with spin centers in 2d hexagonal boron nitride, *arXiv preprint arXiv:2102.10890* (2021).
  - [25] K. Fang, V. M. Acosta, C. Santori, Z. Huang, K. M. Itoh, H. Watanabe, S. Shikata, and R. G. Beausoleil, High-sensitivity magnetometry based on quantum beats in diamond nitrogen-vacancy centers, *Physical review letters* **110**, 130802 (2013).
  - [26] V. M. Acosta, E. Bauch, M. P. Ledbetter, A. Waxman, L.-S. Bouchard, and D. Budker, Temperature dependence of the nitrogen-vacancy magnetic resonance in diamond, *Physical review letters* **104**, 070801 (2010).
  - [27] V. V. Soshenko, V. V. Vorobyov, S. V. Bolshedvorskii, O. Rubinas, I. Cojocaru, B. Kudlatsky, A. I. Zelenev, V. N. Sorokin, A. N. Smolyaninov, and A. V. Akimov, Temperature drift rate for nuclear terms of the nv-center ground-state hamiltonian, *Physical Review B* **102**, 125133 (2020).
  - [28] A. Jarmola, I. Fescenko, V. Acosta, M. Doherty, F. Fatemi, T. Ivanov, D. Budker, and V. Malinovsky, Robust optical readout and characterization of nuclear spin transitions in nitrogen-vacancy ensembles in diamond, *Physical Review Research* **2**, 023094 (2020).
  - [29] M. Barson, P. Reddy, S. Yang, N. Manson, J. Wrachtrup, and M. W. Doherty, Temperature dependence of the c 13 hyperfine structure of the negatively charged nitrogen-vacancy center in diamond, *Physical Review B* **99**, 094101 (2019).
  - [30] X.-D. Chen, C.-H. Dong, F.-W. Sun, C.-L. Zou, J.-M. Cui, Z.-F. Han, and G.-C. Guo, Temperature dependent energy level shifts of nitrogen-vacancy centers in diamond, *Applied Physics Letters* **99**, 161903 (2011).
  - [31] V. M. Acosta, A. Jarmola, L. J. Zipp, M. Ledbetter, E. Bauch, and D. Budker, Broadband magnetometry by infrared-absorption detection of diamond nv centers and associated temperature dependence, in *Advances in Photonics of Quantum Computing, Memory, and Communication IV*, Vol. 7948 (International Society for Optics and Photonics, 2011) p. 79480W.
  - [32] V. Ivády, T. Simon, J. R. Maze, I. Abrikosov, and A. Gali, Pressure and temperature dependence of the zero-field splitting in the ground state of nv centers in diamond: A first-principles study, *Physical Review B* **90**, 235205 (2014).
  - [33] S. Baroni, P. Giannozzi, and A. Testa, Green's-function

- approach to linear response in solids, *Physical review letters* **58**, 1861 (1987).
- [34] R. M. Nieminen, Supercell methods for defect calculations, in *Theory of Defects in Semiconductors*, edited by D. A. Drabold and S. K. Estreicher (Springer Berlin Heidelberg, Berlin, Heidelberg, 2007) pp. 29–68.
- [35] M. Doherty, F. Dolde, H. Fedder, F. Jelezko, J. Wrachtrup, N. Manson, and L. Hollenberg, Theory of the ground-state spin of the nv- center in diamond, *Physical Review B* **85**, 205203 (2012).
- [36] A. Togo, L. Chaput, I. Tanaka, and G. Hug, First-principles phonon calculations of thermal expansion in  $\text{Ti}_3\text{SiC}_2$ ,  $\text{Ti}_3\text{AlC}_2$ , and  $\text{Ti}_3\text{GeC}_2$ , *Physical Review B* **81**, 174301 (2010).
- [37] P. Jacobson and S. Stoupin, Thermal expansion coefficient of diamond in a wide temperature range, *Diamond and Related Materials* **97**, 107469 (2019).
- [38] M. Lax, The franck-condon principle and its application to crystals, *The Journal of chemical physics* **20**, 1752 (1952).
- [39] A. Togo and I. Tanaka, First principles phonon calculations in materials science, *Scr. Mater.* **108**, 1 (2015).
- [40] G. Kresse and J. Furthmüller, Efficient iterative schemes for ab initio total-energy calculations using a plane-wave basis set, *Physical review B* **54**, 11169 (1996).
- [41] G. Kresse and D. Joubert, From ultrasoft pseudopotentials to the projector augmented-wave method, *Physical review b* **59**, 1758 (1999).
- [42] See Supplemental Material for details.
- [43] M. W. Doherty, N. B. Manson, P. Delaney, F. Jelezko, J. Wrachtrup, and L. C. Hollenberg, The nitrogen-vacancy colour centre in diamond, *Physics Reports* **528**, 1 (2013).
- [44] A. Gali, M. Fyta, and E. Kaxiras, Ab initio supercell calculations on nitrogen-vacancy center in diamond: Electronic structure and hyperfine tensors, *Physical Review B* **77**, 155206 (2008).
- [45] O. Vahtras, O. Loboda, B. Minaev, H. Ågren, and K. Ruud, Ab initio calculations of zero-field splitting parameters, *Chemical Physics* **279**, 133 (2002).
- [46] H. M. Petrilli, P. E. Blöchl, P. Blaha, and K. Schwarz, Electric-field-gradient calculations using the projector augmented wave method, *Physical Review B* **57**, 14690 (1998).
- [47] R. K. Defo, E. Kaxiras, and S. L. Richardson, Calculating the hyperfine tensors for group-iv impurity-vacancy centers in diamond using hybrid density functional theory, *Physical Review B* **104**, 075158 (2021).
- [48] J. Gavnholt, T. Olsen, M. Engelund, and J. Schiøtz,  $\Delta$  self-consistent field method to obtain potential energy surfaces of excited molecules on surfaces, *Phys. Rev. B* **78**, 075441 (2008).
- [49] A. Gali, E. Jánzén, P. Deák, G. Kresse, and E. Kaxiras, Theory of spin-conserving excitation of the n- v- center in diamond, *Physical review letters* **103**, 186404 (2009).
- [50] G. Wang, A. Barr, H. Tang, M. Chen, C. Li, H. Xu, J. Li, and P. Cappellaro, Characterizing temperature and strain variations with qubit ensembles for their robust coherence protection (2022), [arXiv:2205.02790](https://arxiv.org/abs/2205.02790).
- [51] J. Zhang, C.-Z. Wang, Z. Zhu, and V. Dobrovitski, Vibrational modes and lattice distortion of a nitrogen-vacancy center in diamond from first-principles calculations, *Physical Review B* **84**, 035211 (2011).
- [52] P. C. Maurer, G. Kucsko, C. Latta, L. Jiang, N. Y. Yao, S. D. Bennett, F. Pastawski, D. Hunger, N. Chisholm, M. Markham, *et al.*, Room-temperature quantum bit memory exceeding one second, *Science* **336**, 1283 (2012).
- [53] A. Dréau, P. Spinicelli, J. Maze, J.-F. Roch, and V. Jacques, Single-shot readout of multiple nuclear spin qubits in diamond under ambient conditions, *Physical review letters* **110**, 060502 (2013).
- [54] J. Shim, I. Niemeyer, J. Zhang, and D. Suter, Room-temperature high-speed nuclear-spin quantum memory in diamond, *Physical Review A* **87**, 012301 (2013).
- [55] M. Abobeih, J. Randall, C. Bradley, H. Bartling, M. Bakker, M. Degen, M. Markham, D. Twitchen, and T. Taminiiau, Atomic-scale imaging of a 27-nuclear-spin cluster using a quantum sensor, *Nature* **576**, 411 (2019).
- [56] G. Thiering and A. Gali, Ab initio magneto-optical spectrum of group-iv vacancy color centers in diamond, *Physical Review X* **8**, 021063 (2018).
- [57] T. Lühmann, R. John, R. Wunderlich, J. Meijer, and S. Pezzagna, Coulomb-driven single defect engineering for scalable qubits and spin sensors in diamond, *Nature communications* **10**, 1 (2019).
- [58] A. Pershin, G. Barcza, Ö. Legeza, and A. Gali, Highly tunable magneto-optical response from magnesium-vacancy color centers in diamond, *npj Quantum Information* **7**, 1 (2021).
- [59] F. A. Zwanenburg, A. S. Dzurak, A. Morello, M. Y. Simmons, L. C. Hollenberg, G. Klimeck, S. Rogge, S. N. Coppersmith, and M. A. Eriksson, Silicon quantum electronics, *Reviews of modern physics* **85**, 961 (2013).
- [60] B. Hensen, W. Wei Huang, C.-H. Yang, K. Wai Chan, J. Yoneda, T. Tanttu, F. E. Hudson, A. Laucht, K. M. Itoh, T. D. Ladd, *et al.*, A silicon quantum-dot-coupled nuclear spin qubit, *Nature nanotechnology* **15**, 13 (2020).
- [61] L. Petit, J. Boter, H. Eenink, G. Droulers, M. Tagliaferri, R. Li, D. Franke, K. Singh, J. Clarke, R. Schouten, *et al.*, Spin lifetime and charge noise in hot silicon quantum dot qubits, *Physical review letters* **121**, 076801 (2018).
- [62] S. Castelletto and A. Boretti, Silicon carbide color centers for quantum applications, *Journal of Physics: Photonics* **2**, 022001 (2020).
- [63] C. Babin, R. Stöhr, N. Morioka, T. Linkewitz, T. Steidl, R. Wörnle, D. Liu, E. Hesselmeier, V. Vorobyov, A. Denisenko, *et al.*, Fabrication and nanophotonic waveguide integration of silicon carbide colour centres with preserved spin-optical coherence, *Nature materials* **21**, 67 (2022).
- [64] C. P. Anderson, E. O. Glen, C. Zeledon, A. Bourassa, Y. Jin, Y. Zhu, C. Vorwerk, A. L. Crook, H. Abe, J. Ull-Hassan, *et al.*, Five-second coherence of a single spin with single-shot readout in silicon carbide, *Science advances* **8**, eabm5912 (2022).
- [65] T. Zhong, J. Rochman, J. M. Kindem, E. Miyazono, and A. Faraon, High quality factor nanophotonic resonators in bulk rare-earth doped crystals, *Optics express* **24**, 536 (2016).
- [66] C. Le Gall, Clock qubit conducts nuclear ensemble, *Nature Physics* , 1 (2022).
- [67] A. Ruskuc, C.-J. Wu, J. Rochman, J. Choi, and A. Faraon, Nuclear spin-wave quantum register for a solid-state qubit, *Nature* **602**, 408 (2022).
- [68] J. P. Perdew, K. Burke, and M. Ernzerhof, Generalized gradient approximation made simple, *Physical review letters* **77**, 3865 (1996).

- [69] H. J. Monkhorst and J. D. Pack, Special points for brillouin-zone integrations, *Physical review B* **13**, 5188 (1976).



## DETAILS OF FIRST-PRINCIPLES CALCULATION

The electronic structure calculation employs the projector-augmented-wave (PAW) method implemented by the Vienna ab-initio simulation package (VASP) with a cut-off energy of 520 eV [40, 41]. Spin-unrestricted calculations are implemented using the generalized gradient approximation (GGA) with the Perdew-Burke-Ernzerhof (PBE) functional for electron exchange-correlation [68] in the calculation of atomic relaxation, density functional perturbation theory (DFPT),  $D$ ,  $Q$ , and  $A$  matrix. The  $k$ -point mesh is sampled by the Monkhorst-Pack method [69] with a separation of  $0.2 \text{ rad}/\text{\AA}^{-1}$  ( $3 \times 3 \times 3$   $k$ -point mesh in the supercell). The energy of electronic iterations converge to  $10^{-7}$  eV and force on atoms converge to  $0.01 \text{ eV}/\text{\AA}$ .

The phonon calculation is implemented in the  $4 \times 4 \times 4$  rhombohedral supercell with only  $\Gamma$   $k$ -point. 381 phonon modes are obtained at  $\Gamma$   $k$ -point, including 3 trivial modes corresponding to overall translation. The trivial modes have no contribution to Eq. (5) in the main text, as the overall translation of the system does not change any transition energy. All the 378 non-trivial phonon modes are then used to calculate the second-order derivative according to Eq. (5) in the main text. In Eq. (5), the step of displacement  $\delta q_i$  is set as  $0.1 \text{ \AA}$  in the NV center calculation. We tested that using  $\delta q_i = 0.05 \text{ \AA}$  gives almost the same temperature dependence, confirming the convergence of our results to  $\delta q_i$ . We mention that numerically,  $\delta q_i = 0.1 \text{ \AA}$  is not a large value as it appears to be, as this magnitude of displacement is distributed to all the 127 atoms in the supercell, and the displacement of each atom is in a proper range.

### CALCULATION OF $D$ , $Q$ , AND $A$

The first term in Eq. (6) in the main text originates from the electron spin-spin magnetic dipolar interaction from the Kohn-Sham orbitals [32]:

$$D_{ij} = \frac{\mu_0 g_e^2 \mu_B^2}{4\pi} \sum_{a < b} \chi_{ab} \left\langle \Psi_{ab} \left| \frac{r^2 \delta_{ij} - 3r_i r_j}{r^5} \right| \Psi_{ab} \right\rangle \quad (\text{S1})$$

where  $\mu_0$ ,  $\mu_B$ ,  $g_e$  are the magnetic constant, Bohr magneton, and Landé factor of electron, respectively. The summation goes through all electron pairs  $(a, b)$ .  $\Psi_{ab}$  are particle determinant wave functions from the Kohn-Sham ground state and  $\chi_{ab}$  equals  $+1/-1$  when the states  $a$  and  $b$  have the same/different spin.

The hyperfine constant (the 2<sup>nd</sup> term in Eq. (6) in the main text) is a summation of the Fermi contact contribution and dipolar contribution:

$$A_{ij} = \frac{\mu_0 g_e g_I \mu_B \mu_I}{\langle S_z \rangle} \times \left[ \frac{2}{3} \delta_{ij} \rho_s(\mathbf{R}_I) + \frac{1}{4\pi} \int \frac{\rho_s(\mathbf{r} + \mathbf{R}_I)}{r^3} \frac{3r_i r_j - \delta_{ij} r^2}{r^2} d\mathbf{r} \right] \quad (\text{S2})$$

where  $g_I$ ,  $\mu_I$ , and  $R_I$  are the g-factor, nuclear magneton, and coordinate of nuclear spin,  $\rho_s$  is the electron spin density from the DFT ground state. In the NV center calculation, we use the g-factor of  $g_I = 3.077 \times \frac{h}{\mu_B}$  MHz/T for  $^{14}\text{N}$  and  $g_I = 10.7084 \times \frac{h}{\mu_B}$  MHz/T for  $^{13}\text{C}$ .

The nuclear quadrupole interaction is calculated through the electric field gradient (EFG)  $V_{ij} = \partial_i E_j$  from the electron density  $\rho(r)$ :

$$V_{ij} = \frac{e}{4\pi\epsilon_0} \left[ - \int \rho(r + R_I) \frac{3r_i r_j - \delta_{ij} r^2}{r^5} dr + \sum_{I'} Z_{I'} \frac{3R_{II',i} R_{II',j} - \delta_{ij} R_{II'}^2}{R_{II'}^5} \right] \quad (\text{S3})$$

where  $e$ ,  $\epsilon_0$ ,  $Z_{I'}$ ,  $R_I$ , and  $R_{II'}$  are the electron charge, vacuum dielectric constant, nuclear charge, position of nucleus, and relative coordinate between nucleus  $I'$  and  $I$ . The  $Q$  matrix is then calculated by the three principal axis system (PAS) eigenvalues  $V_{1,2,3}$  of the EFG:

$$Q_{ij} = \frac{eQ_I}{4I(2I-1)} \begin{bmatrix} V_1 - V_2 - V_3 & 0 & 0 \\ 0 & -V_1 + V_2 - V_3 & 0 \\ 0 & 0 & 2V_3 \end{bmatrix} \quad (\text{S4})$$

where  $Q_I$  is the nuclear quadrupole moment. In the NV center calculation, we use the  $^{14}\text{N}$  nuclear quadrupole moment  $Q_I = 20.44 \text{ e}\cdot\text{mb}$ .

In the principal axis coordinates, Eq. (6) in the main text is converted to:

$$\hat{H}_D = D[S_z^2 - \frac{1}{3}S(S+1) + \frac{\epsilon}{3}(S_+^2 + S_-^2)] \quad (\text{S5})$$

$$\hat{H}_Q = Q[I_z^2 - \frac{1}{3}I(I+1) + \frac{\eta}{3}(I_+^2 + I_-^2)] \quad (\text{S6})$$

$$\hat{H}_A = A_{zz}S_zI_z + A_{xx}S_xI_x + A_{yy}S_yI_y \quad (\text{S7})$$

where  $D = \frac{3}{2}D_{zz}$  and  $Q = \frac{3}{2}Q_{zz}$  are the splitting energy, and  $\epsilon = (D_{xx} - D_{yy})/D_{zz}$  and  $\eta = (Q_{xx} - Q_{yy})/Q_{zz}$  are the asymmetric coefficients. Applying to an uniaxial system like NV-center under zero strain, we select the  $C_3$  axis as  $z$ -direction and the effective Hamiltonian reduces to (considering  $H_D \gg H_A, H_Q$ ) Eq. (7) in the main text.

### CALCULATION OF THE TEMPERATURE-DEPENDENT ZPL

Although the ZPL is not spin-transition, its temperature dependence can be calculated by the same theoretical framework. The only difference is that the energy levels of the excited state and ground state have a large separation of 1.945 eV, so their difference can no longer be evaluated perturbatively. Compared with the spin transition where the transition energy is far smaller than the phonon energy, here the electronic transition energy is far larger than the phonon energy.

The calculation is implemented through evaluating Eq. (4) in the main text. At first, we use the  $\Delta$  SCF method [48] to calculate the relaxed atomic structure and electronic structures of the excited states, where one electron is placed in a high-lying Kohn-Sham orbital. In the NV center calculation, this is realized by fixing the electron occupancy according to the  $^3E$  excited state's  $a_1e^3$  molecular orbital configuration as in ref. [49]. (The same electron occupancy is set for all  $k$  points in the supercell calculation, yielding the  $^3E$  state with one excited electron in each NV center, or namely, one excited electron in each supercell). The phonon spectral of the excited states is then calculated, deriving a series of excited state phonon frequency  $\omega_i^e$ . Combining with the ground state phonon frequency  $\omega_i^g$ , we derive  $\Delta\omega_i$  in Eq. (4) in the main text.  $\omega_i$  in the equation is set as the ground state phonon frequency, as phonon exhibits the Boson distribution according to the ground state phonon spectral in the ZPL measurement. The first-order contribution from  $\nu_0(T)$  is directly calculated through the excitation energy calculation under lattice expansion by the  $\Delta$  SCF method.

### CONVERGENCE TEST OF THE SUPERCELL SIZE

Here we conducted convergence test to show that the 127-atom  $4 \times 4 \times 4$  rhombohedral supercell we used for NV centers can derive temperature dependence reasonably convergent against supercell size. The temperature dependence of  $A_{zz}$  and  $Q$  is calculated by both the 127-atom supercell and a 216-atom cubic supercell, as shown in Fig. S1. The temperature dependence calculated by different supercell is well consistent, supporting that the 127-atom supercell can derive temperature dependence with reasonable convergence. As the computational cost of the temperature dependence calculation grows dramatically with the supercell size, we recommend the 127-atom supercell based on our test results to people who intend to use our method.

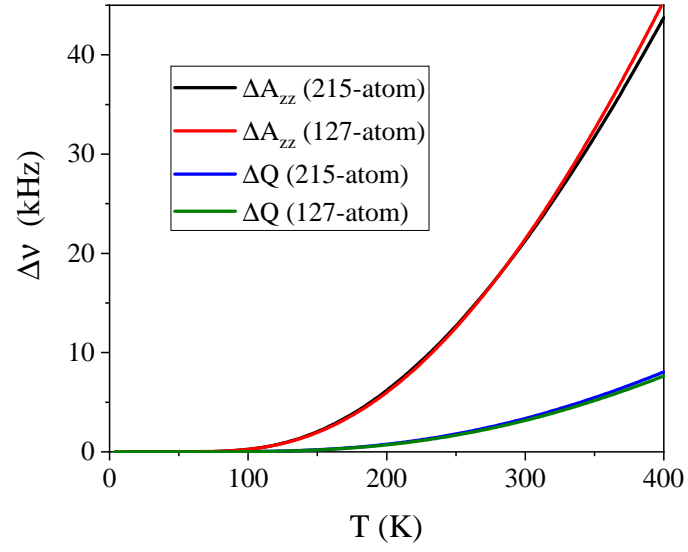


FIG. S1. Convergence test of the temperature dependence of  $A_{zz}$  and  $Q$  of the  $^{14}\text{N}$  nuclear spin in NV centers. The black/blue and red/green curves represent the temperature drifts of  $A_{zz}/Q$  of the  $^{14}\text{N}$  atom calculated by the 215-atom rhombohedral supercell and 127-atom cubic supercell, respectively